MICROROBOTS

A microrobotic platform actuated by thermocapillary flows for manipulation at the air-water interface

Franco N. Piñan Basualdo[1,2]*, A. Bolopion[2], M. Gauthier[2], P. Lambert[1]

Future developments in micromanufacturing will require advances in micromanipulation tools. Several robotic micromanipulation methods have been developed to position micro-objects mostly in air and in liquids. The air-water interface is a third medium where objects can be manipulated, offering a good compromise between the two previously mentioned ones. Objects at the interface are not subjected to stick-slip due to dry friction in air and profit from a reduced drag compared with those in water. Here, we present the ThermoBot, a microrobotic platform dedicated to the manipulation of objects placed at the air-water interface. For actuation, ThermoBot uses a laser-induced thermocapillary flow, which arises from the surface stress caused by the temperature gradient at the fluid interface. The actuated objects can reach velocities up to 10 times their body length per second without any on-board actuator. Moreover, the localized nature of the thermocapillary flow enables the simultaneous and independent control of multiple objects, thus paving the way for microassembly operations at the air-water interface. We demonstrate that our setup can be used to direct capillary-based self-assemblies at this interface. We illustrate the ThermoBot's capabilities through three examples: simultaneous control of up to four spheres, control of complex objects in both position and orientation, and directed self-assembly of multiple pieces.

INTRODUCTION

Most of the research aiming to develop microrobotic platforms target two main media: air and liquid. However, microrobotic tools have recently been developed to work at the air-water interface (*1*–*4*). Micromanipulation at the interface profits from a reduced drag compared with the liquid bulk, and it is not subjected to dry friction inducing the stick-slip motion usually seen in dry environments (*5*). Moreover, at submillimetric scales, surface tension becomes substantial, for instance, allowing objects denser than water to float. In this article, we therefore propose the ThermoBot: a noncontact manipulation platform working at the air-water interface and based on surface tension effects. The proposed setup can be used to stimulate the self-assembly (*6*) of floating objects, thereby paving the way for the development of micromanufacturing operations at the air-water interface.

Different actuation methods have been developed at the air-water interface, among which rower robots, magnetic actuation, and surface tension–based actuation are the most common ones. Rower robots, inspired by insects, use the drag force to propel themselves (*7*–*10*). This kind of robot can easily be controlled, but the actuators must be placed on the floating robots themselves, making them complex to miniaturize below the centimeter scale. To avoid having to use embedded actuators, the most common alternative is magnetic actuation by an externally controlled magnetic field. Magnetic actuation has been proven to allow a precise position control at the air-water interface (*1*, *5*, *11*, *12*), but it requires materials with specific magnetic properties. In addition, magnetic actuation is adequate to control swarms where all agents are subjected to similar actuation forces, but the multi-object control is challenging because all the agents are affected by the same magnetic field. Recently, researchers have achieved magnetic multi-object control, using additional physical effects (*13*), the different dynamic response of the agents (*14*), or spatially selective actuation (*15*). The third actuation option at the air-water interface is to directly exploit the surface tension, a substantial effect at the microscale.

Surface tension is a property of the interface (here the air-water interface) that can be considered an excess of energy at the surface (*16*), making the interface behave similarly to an elastic membrane. Therefore, interfaces develop a restoring force when deformed by an object, making it possible for objects denser than water to float (*17*). Furthermore, in the presence of a gradient of surface tension, low–surface tension areas (low excess energy) tend to expand toward high–surface tension areas (minimizing the excess energy), thereby giving rise to convective flows. This effect, known as the Marangoni effect (*18*), can be used to propel floating objects through a surface tension gradient. One option to generate such a gradient is to locally decrease the surface tension using solvents or surfactants (solutocapillary actuation), as some insects do to rapidly escape predators (*19*). This technique is appealing because it induces high speeds (*2*, *4*, *20*–*23*) and does not require any external source of energy. However, increasing the life span is challenging because of fuel depletion and surface saturation. The control of the propulsion direction requires additional physical effects. Another option is to locally decrease the surface tension by heating the air-water interface (thermocapillary actuation), thereby generating a convective flow at the interface from hot to cold areas. This effect has already been exploited to manipulate bubbles (*24*) and cells (*25*) in the liquid bulk and droplets (*26*) and solid spheres (*27*) at the interface. We demonstrate that this physical effect can also be used to control objects placed at the interface in both position and orientation, opening the possibility for the development of a microrobotic platform able to perform microassembly operations.

In this paper, we present ThermoBot: a microrobotic platform using thermocapillary actuation to manipulate objects at the air-water interface. The thermocapillary flow is generated by heating the air-water interface with an infrared laser, thereby conveying the floating objects away from the laser spot. The objects are then controlled by displacing the laser spot around them. Because the objects are propelled by the flow, they can be of any shape and material as long

[1]Transfers Interfaces and Processes (TIPs), Ecole Polytechnique de Bruxelles (CP 165/67), Université Libre de Bruxelles, 1050 Brussels, Belgium. [2]FEMTO-ST Institute, CNRS, Univ. Bourgogne Franche-Comté, 24 rue Savary, F-25000 Besançon, France. *Corresponding author. Email: franco.pinan.basualdo@ulb.be

as they float. The attained velocities are only surpassed by those of solutocapillary-based actuation (fig. S1); however, ThermoBot allows us to control the displacement direction, among other advantages (table S1). The ThermoBot's actuation principle offers a promising route for a robotic platform enabling micromanufacturing operations at the air-water interface (Fig. 1). At this interface, lateral capillary forces (*28*, *29*) enable the self-assembly of floating objects (*12*, *30*, *31*); therefore, we propose ThermoBot as a way to actively control such assemblies. ThermoBot not only speeds up the self-assembly or prevent defaults but also allows us to purposely drive the system to a metastable assembly. On the basis of an accurate knowledge of the ThermoBot actuation principle, we experimentally demonstrate the following capabilities: simultaneous control of multiple spheres, control of a multiple-legged object in both position and orientation, and directed self-assembly.

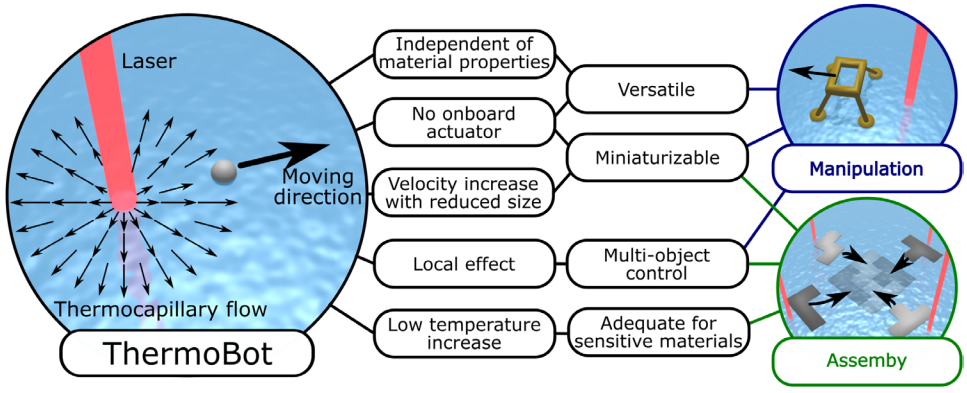

Fig. 1. Sketch and diagram showing ThermoBot's main characteristics. ThermoBot constitutes a micromanipulation tool and paves the way for micromanufacturing operations at the air-water interface.

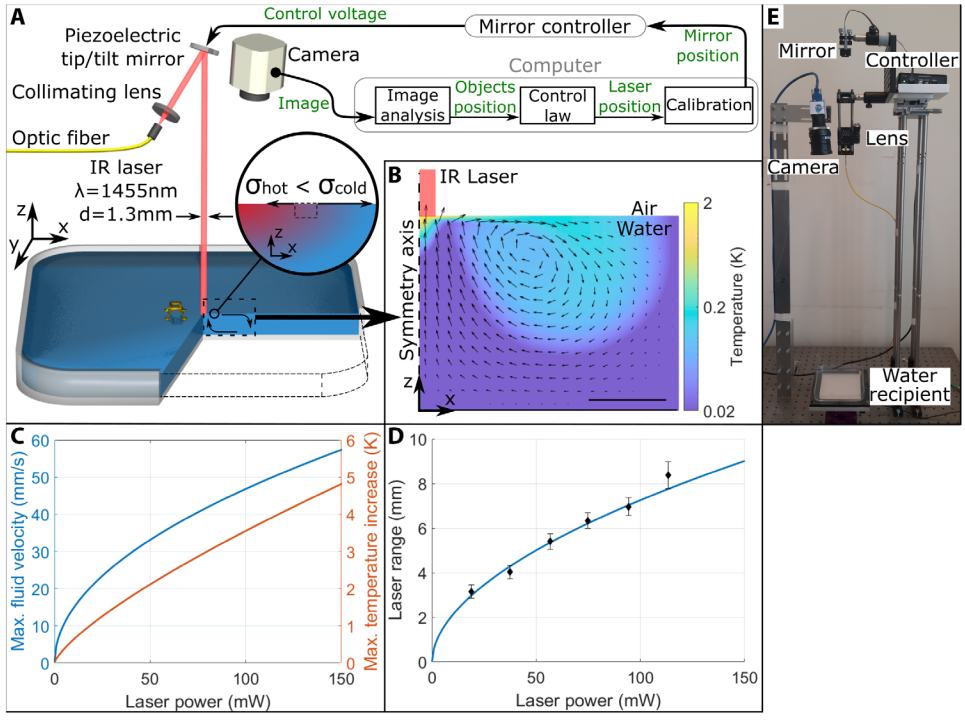

Fig. 2. ThermoBot microrobotic platform. (**A**) Schematics of system control loop from image acquisition to mirror control and the laser-induced thermocapillary effect. For animation, see movie S1. (**B**) Flow simulation results for a laser power of 50 mW. The color map represents the temperature, and the arrows represent the flow velocity (both are in logarithmic scales because the values at the surface are much higher than in the bulk). Scale bar, 3 mm. (**C**) Flow simulation results: maximum temperature increase (at the interface and at the center of the laser beam) and maximum fluid velocity (at the interface and at around 1 mm from the laser beam) as a function of the laser power. (**D**) Range of the laser effect: flow simulations results (see section B of the Supplementary Materials for more details) and measurements performed by spreading aluminum flakes (typical size of 70 μm on the interface) and measuring how far they are repelled by the flow. The error bars represent the range (difference between highest and lowest value) of three measurements. (**E**). Photo of the experimental setup.

RESULTS

ThermoBot actuation system

ThermoBot actuates floating objects through a laser-induced thermocapillary flow. The actuation system consists in pointing an infrared laser beam at a water volume whose top surface is in contact with air (Fig. 2A). The water will absorb the laser energy, which locally increases the temperature (T) and, because of the surface tension (σ) variation with temperature (fig. S2A), decreases the surface tension. Thanks to the Marangoni effect (*18*), this surface tension gradient creates a convective flow, known as thermocapillary flow. This effect can be conceptually understood by considering a volume of fluid just below the interface that, owing to the surface tension gradient, will undergo a net attraction toward high–surface tension (i.e., colder) regions. This force is balanced by the shear stress with lower fluid layers, and this equilibrium is written mathematically as

$$\mu \frac{\partial \mathbf{U}}{\partial \mathbf{n}} = -\nabla_S \sigma = -\frac{\partial \sigma}{\partial T} \nabla_S T \qquad (1)$$

where $\mathbf{U}$ is the fluid velocity vector, $\mathbf{n}$ is a unit vector normal to the interface that points down toward the water phase, μ is the fluid's dynamic viscosity, and ∇_S is the surface gradient operator $[\nabla_S f = \nabla f - \mathbf{n}(\mathbf{n}\cdot\nabla f)]$. In the temperature range within which we are operating, we can consider a constant value $\partial\sigma/\partial T \approx -155$ μN/(mK) (fig. S2A). In our setup, we used an infrared laser (wavelength λ = 1455 nm) that was collimated to obtain a 1.3-mm-diameter spot at the interface. The main advantage of using a laser as an energy source is that

even with a moderate laser power (up to 150 mW), we obtain a high power density (up to 250 mW/mm^2) compared with other heating mechanisms. We performed numerical simulations of the flow (section B of the Supplementary Materials) and observed that the generated flow is a toroidal convection cell around the laser spot (Fig. 2B). The high power density of the laser generates high temperature gradients (up to 3500 K/m), leading to high fluid velocities (up to 60 mm/s), with relatively small temperature increases (peak temperature up to 5 K) (Fig. 2C). Notice that the laser power is low compared with the total heat capacity of the water volume (average temperature increase limited to 70 mK/min). Once onset, this thermocapillary flow conveys floating objects away from the laser spot. The laser range (radius of the area affected by the flow) was also estimated trough simulations and measured experimentally (Fig. 2D). It was observed to vary from 3 mm for a laser power of 20 mW to 9 mm for a laser power of 150 mW. Therefore, although increasing the laser power would increase the effect, it would also increase the area affected by the laser, thus making it harder to independently control multiple objects.

The actuation system is completed by a piezoelectric tip/tilt mirror capable of steering the laser spot on the interface and a camera used to close the control loop (Fig. 2A). The mirror rotation limits and its distance to the interface result in an 80-mm by 80-mm workspace, whereas its fast dynamics (response time around 2 ms) allow the multiplexing of the laser beam (section C of the Supplementary Materials), to simultaneously control multiple objects or to use multiple laser spots to control a complex object. We used the laser spot position as the control variable, allowing us to perform complex operations without having to vary the laser power (although we did change the laser power between experiments).

Simultaneous control of multiple spheres

First, we demonstrate the simultaneous and precise control of multiple spheres (Fig. 3A). In this experiment, we displaced 500-μm-diameter steel spheres able to float at the air-water interface thanks to the surface tension (*17*). When the laser spot was kept at a constant distance from the sphere, the latter accelerated until reaching a steady velocity depending on the laser-sphere distance and on the laser power (Fig. 3B). By multiplexing the laser, we simultaneously steered two spheres along a closed path (Fig. 3D) using a self-developed closed-loop path-following technique (section D of the Supplementary Materials). The technique successfully kept the sphere on the path, with an error of up to 0.9 mm and a mean error of 0.2 mm after the initial approach (Fig. 3C). As another example of the ThermoBot's capabilities, four spheres were simultaneously controlled, first separating them and then rotating them clockwise (Fig. 3E). In the last experiment, no path was prescribed; instead, there was a moving target for each sphere.

Multiple-legged object control

Being able to multiplex the laser spot also enables the control of complex objects, such as a multiple-legged one (Fig. 4A). Although in this experiment the object was about 50 times heavier than the steel spheres, we could still obtain rotation and locomotion speeds

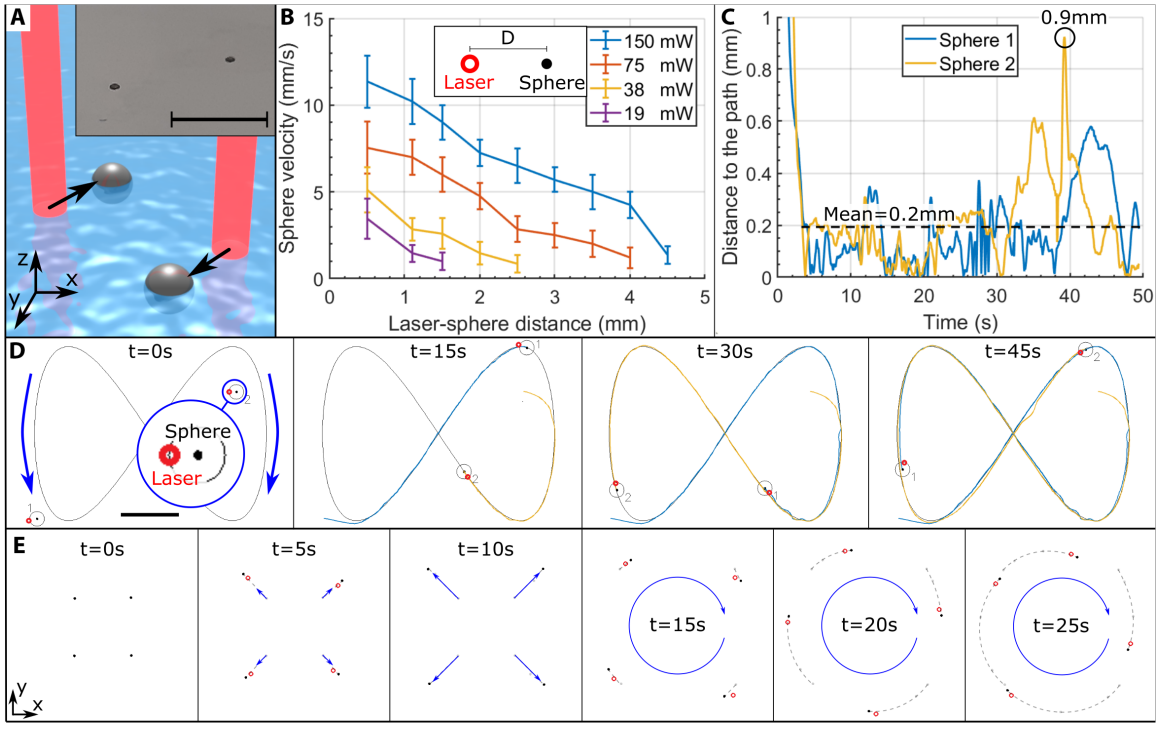

Fig. 3. Simultaneous control of multiple spheres. (**A**) Schematics of two spheres being controlled independently. The inset is a macro photograph of two spheres (scale bar, 5 mm). (**B**) Experimental characterization of sphere steady-state velocity as a function of the laser-sphere distance and the laser power. The error bars represent the range (difference between highest and lowest value) of eight measurements. (**C**) Experimental sphere-path distance evolution of the path-following experiment shown in (D). (**D**) Experimental simultaneous control of two spheres following a path (Lissajous curve $x = 20\cos(\alpha)$ [mm] and $y = 15\sin(2\alpha)$ [mm] with $0 \leq \alpha < 2\pi$). A circle was added digitally around each of the spheres to make them easier to identify, the red circles represent the laser spots, and the blue and yellow lines represent the spheres' trajectories. Scale bar, 10 mm. See movie S2. (**E**) Experimental simultaneous control of four spheres. Same scale as (D). See movie S3.

of up to 80°/s and 8 mm/s, respectively, by using two laser spots (Fig. 4B). On the basis of these experiments, we developed a simple model (fig. S2) allowing us to estimate the robot's motion for any relative laser spot position. By placing each of the laser spots at a different distance from their leg, we could combine control of both translation and rotation of the object to make it follow a path (Fig. 4D). In this configuration, the robot's dynamics constitute a nonholonomic system (*32*) for which a controller was specifically developed (section E of the Supplementary Materials). ThermoBot made the objects follow the path with an error of up to 2.6 mm and a mean error of 1.2 mm (Fig. 4C).

Directed self-assembly

ThermoBot constitutes an alternative tool for micromanufacturing at the air-water interface. It can be used to direct the self-assembly of objects at the interface, where the self-assembly is enabled by lateral capillary forces (Fig. 5, A and B). Lateral capillary forces are interactions between floating objects (responsible for the clumping of breakfast cereals on the surface of a bowl of milk) that result from a minimization of surface and gravitational energy (*28*, *29*). Although the capillary interactions can be tuned during the manufacturing of parts by adjusting their wetting properties (*30*) or their geometry (*31*), defects can still occur because of metastable states (local minimum energy configuration that is not the global minimum) and unfavorable initial positions. Moreover, because the strength of lateral capillary forces strongly decreases with distance, if the parts are initially far apart, the initial approach can be slow. These problems can be solved by adding active particles to the interface to direct the assembly (*12*), but these particles can also interfere with the assembly. Therefore, we propose to use ThermoBot to actively direct capillary-based self-assemblies. It can be used to approach the parts with any desired orientation, preventing defects and speeding up the process. It can even rectify assembly defects by first separating the parts (section F of the Supplementary Materials) and then letting them reassemble properly. We successfully used ThermoBot to perform the self-assembly of U-L-B (Fig. 5C) and house-like (Fig. 5D) puzzles.

For some applications, it might be interesting to drive the assembly to a metastable state, something that requires an active way to control the assembly. We have developed an automatic controller allowing us to purposely drive a system of two "C" shape pieces to a metastable state (Fig. 6, A and B) using ThermoBot. In this case, an automatic controller was necessary because both particles are controlled simultaneously to approach each other with the desired orientation. The technique consists in rotating both particles to face one another and then approaching them toward each other. We repeated this experiment 31 times, and the assembly failed only once. We attribute this failure to the fact that the particles were initially too close to each other for the controller to compensate for the error in orientation. The results for the other 30 experiments are summarized in Table 1. This technique can easily be extended to assemble more pieces if they can be assembled in series (one piece added to the assembly at the time). However, it can be harder to implement when the simultaneous assembly of more than two pieces is needed, because the final approach is very fast and dominated by capillary forces, making it impossible to keep the orientation controlled.

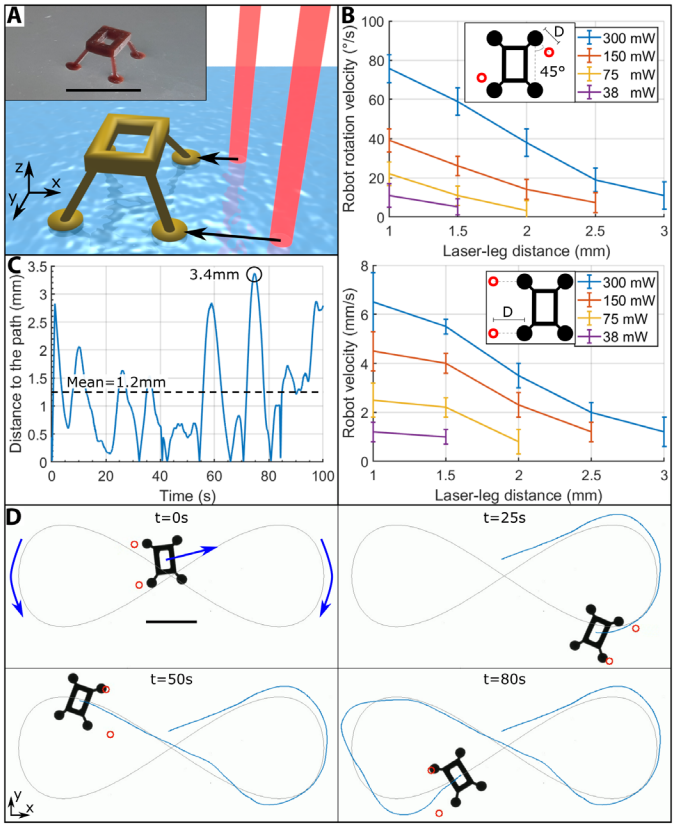

Fig. 4. Multiple-legged object control. (**A**) Sketch of a floating object with four legs controlled by laser-induced thermocapillary flow. The inset is a photo of an object (scale bar, 10 mm). (**B**) Object rotation and displacement characterization as a function of the laser-leg distance and the total laser power. The error bars represent the range (difference between highest and lowest value) of three measurements. (**C**) Experimental robot-path distance evolution of the path-following experiment shown in (D). (**D**) Experimental simultaneous orientation and position control of a four-legged object following a path (Lissajous curve $x = 30\sin(2\alpha)$ [mm] and $y = 10\cos(\alpha)$ [mm] with $0 < \alpha < 2\pi$). The red circles represent the laser spots, and the blue line represents the object trajectory. Scale bar, 10 mm. See movie S4.

DISCUSSION

In this article, we presented the ThermoBot, a microrobotic platform dedicated to the manipulation of objects placed at the air-water

Table 1. Automatic metastable assembly results. The error was measured normal to the line joining the two pieces by analyzing the images taken during the assembly (camera resolution of 80 μm). The time was measured between the moment the algorithm was launched and the moment the final assembly was achieved.

	Number of occurrences	Error(μm)			Total
		[0,100]	(100,200]	(200,300]	
Time (s)	[10, 20]	18	4	1	23
	(20,30]	4	1	0	5
	>30	2	0	0	2
	Total	24	5	1	30

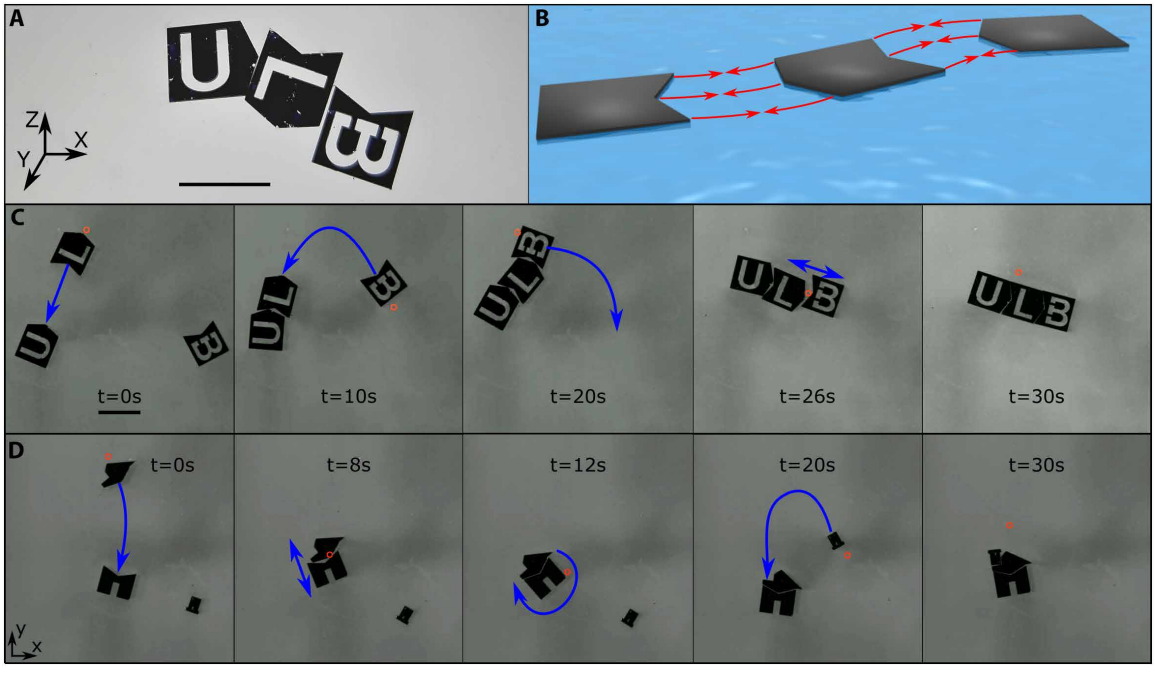

Fig. 5. Directed self-assembly. (**A**) Photo of failed self-assembly (scale bar, 10 mm). (**B**) Schema of lateral capillary forces promoting self-assembly between pieces. (**C**) Experimental directed assembly of a U-L-B puzzle. The red circle represents the laser spot. Scale bar, 10 mm. See movie S5. (**D**) Experimental directed assembly of a house puzzle. Same scale as (C). See movie S6.

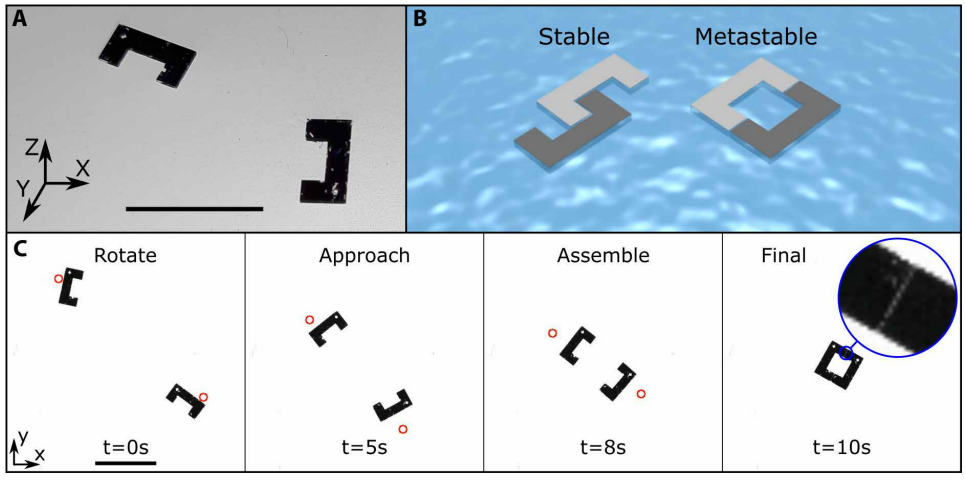

Fig. 6. Automatic metastable assembly of "C" shape pieces. (**A**) Photo of two C shape pieces (scale bar, 10 mm). (**B**) Schema showing a stable (left) and a metastable (right) assembly of two C shape pieces. (**C**) Experimental automatic assembly of two C shape pieces purposely driven to a metastable configuration. The red circles represent the laser spots. Scale bar, 10 mm. See movie S7.

interface. The actuation system is based on the generation of a thermocapillary flow, a flow that arises from an interface temperature gradient thanks to the Marangoni effect (*18*). We generated this temperature gradient by pointing an infrared laser at the interface, which generated a flow that propelled floating objects away from the laser spot. By repositioning the laser spot using a piezoelectric tip/tilt mirror, we were able to control the object displacement. The laser's high power density allows the object to attain velocities of up to 12 mm/s (24 body lengths/s) with very low temperature increases (up to 5 K), making our system suitable for actuating sensitive components, such as electronic components. Moreover, our system does not require any on-board actuators, and it does not rely on any specific material properties, therefore making ThermoBot a highly versatile system. Furthermore, the localized nature of the thermocapillary flow enables the simultaneous and independent control of multiple objects. All of these are the key features behind ThermoBot's capacity to perform controlled operations at the air-water interface. One of these operations is the direction of capillary-based self-assemblies, allowing ThermoBot to purposely drive the assembly to a metastable state and preventing defaults and hopefully paving the way for the emergence of micromanufacturing applications. It should also be noted that, because the objects' speeds become independent of size at small scales (theoretically, a massless point particle speed would be equal to the fluid velocity), scaling down the proposed setup could be an appealing actuation alternative at the micro- and nanoscales.

In addition to the wide range of applications already presented in this article, we would like to mention further ways of exploiting our system's capabilities. With our current setup, we were able to effectively multiplex the laser up to a maximum of five laser spots; this number was limited mainly by the mirror speed. One way to further increase this number could be to make use of a spatial light modulator (*24*). This would allow us not only to increase the number of laser spots but also to create an almost arbitrary illumination pattern, leading to complex flows and allowing the study of alternative control techniques.

MATERIALS AND METHODS

ThermoBot's actuation system

Our setup can be subdivided into four different subsystems:

1) Optical system. We used an infrared (IR) laser source (Keopsys Fiber Raman Laser CRFL-01-1455-OM1-B130-FA) with a wavelength λ = 1455 nm and an output power from 40 mW to 1 W to locally heat the water. The source output was connected using an optic fiber (Thorlabs SM980-5.8-125) to a fiber adapter (Thorlabs HAFC - FC/PC) in front of which we placed a collimating lens (Thorlabs Lens A110TM) with a focal length f = 6.24 mm. According to the supplier, the optic fiber mode field diameter (MFD) for our wavelength is MFD = 8.8 μm, obtaining an output beam diameter of $d \approx 4\lambda f/(\pi \mathrm{MFD})$ = 1.3 mm. The total efficiency of the optical system was measured to be around 50%; therefore, the power reaching the interface can be varied between 20 and 500 mW.

2) Mirror system. After being collimated, the laser beam reflected on a piezoelectric tip/tilt mirror (Mirrorcle A7M20.2-2000AL-DIP24-C/TP), which was located at about 80 cm from the interface. The mirror maximum rotation angles are ±5°, resulting in a maximum workspace of 140 mm by 140 mm, but we limited it to 80 mm by 80 mm because the mirror behavior for high deflection angles is not linear. The mirror orientation was controlled by its own controller (Mirrorcle MEMS Controller USB-SL MZ), which was connected to the computer via USB (universal serial bus). This controller generates the high-voltage signals required to control the piezoelectric mirror and has an internal filter to protect the mirror from abrupt movements.

3) Water system. We used a 125-mm by 125-mm by 15-mm polyethylene container filled with an 8-mm-deep layer of distilled water (100 cm^3). The recipient was cleaned with ethanol and then rinsed with distilled water before each experiment. The distilled water we used was obtained from the Arium pro Ultrapure Water Systems, which, according to the supplier, has a quality superior to the ASTM (American Society for Testing and Materials) type 1 water quality standard.

4) Vision system. We used an IDS camera USB 3.0 UI-3370CP with the Navitar Lens NMV-75M1 for vision. The camera was configured for a resolution of 1024 pixels by 1024 pixels and the frame rate was 20 frames per second. The camera was placed at around 80 cm from the interface, resulting in a field of view of 80 mm by 80 mm (13 pixels/mm). To be able to accurately identify the object's position from the images, a white back light (PHLOX LEDW-BL-100x-LLUB-Q-1R-24V) was placed below the water recipient to saturate the camera and make it easier to digitally analyze the image. This back light was used when the automatic object detection was necessary, thus explaining the white background in Figs. 3, 4, and 6, but it was not necessary when the laser position was imposed by the user (Fig. 5).

Last, all the above-described elements, except for the laser and water sources, were placed on top of an antivibration table (Newport VH3030W-OPT) to reduce noise during the experiments.

Mirror calibration

To find the adequate mirror rotation to obtain a desired laser position in the camera frame (calibration box in Fig. 2A), a preliminary calibration step is necessary. Because the IR laser is not visible to the camera, a visible red laser (Visual Fault Locator TL532) was coupled with the IR laser in the optic fiber using a laser coupler (Thorlabs WD202C-APC). To be able to see the red laser spot, the water recipient was replaced with a white paper surface at approximately the position of the air-water interface. Next, a calibration step, where only the red laser was on, was performed by varying the mirror position along both axes and recording the obtained laser spot position in the camera frame. Last, a third-degree two-dimensional polynomial fitting was performed, defining the required mirror position for a desired laser position (calibration box in Fig. 2A). The calibration was also corroborated using the IR laser and a laser viewing card (Thorlabs VIS/NIR Detector Card). The calibration was checked every day before performing experiments and repeated if necessary.

Software

We wrote a custom C code using the Qt widget toolkit to control the system. We used the provided software development kits to communicate with the camera and the mirror controller. When launched, the software set the camera configuration and began the image acquisition. Upon the reception of each frame, an image analysis routine based on the OpenCV 2.4.11 was performed. First, the position and orientation of the floating objects were found using the OpenCV contours function. Second, a control law routine or the user input was used to determine the desired laser spot position. Third, the previously described mirror calibration was used to find the necessary mirror position that was lastly sent to the mirror controller. Each frame, the objects' positions, the laser positions, other auxiliary data, and, optionally, the received images were saved.

Controlled objects

The spheres shown in Fig. 3A had a 0.5-mm diameter, were made of AISI 420C stainless steel, and were supplied by Redhill Precision. The multiple-legged object shown in Fig. 4A was made using a Digital Light Printing technique operated at the Laboratoire Interdisciplinaire de Physique (LIPhy). The self-assembly parts shown in Figs. 5A and 6A were made of fused silica, were 0.5 mm thick, were cut with FEMTOPrint, and were painted with black permanent marker to make them opaque.

SUPPLEMENTARY MATERIALS

robotics.sciencemag.org/cgi/content/full/6/52/eabd3557/DC1

Text

Fig. S1. Comparison between ThermoBot and other microrobotic platforms working at the air-water interface.

Fig. S2. Thermocapillary flow simulation.

Fig. S3. Laser multiplexing.

Fig. S4. Spheres model and control simulations.

Fig. S5. Multiple-legged object model and control simulations.

Fig. S6. Forces acting on self-assembled objects and their separation.

Table S1. Comparison between rower robots, magnetic actuation, solutocapillary-based actuation, and ThermoBot actuation.

Movie S1. Setup presentation.

Movie S2. Experimental simultaneous control of two spheres following a path.

Movie S3. Experimental simultaneous control of four spheres.

Movie S4. Experimental simultaneous orientation and position control of a four-legged object following a path.

Movie S5. Experimental directed assembly of a U-L-B puzzle.

Movie S6. Experimental directed assembly of a house puzzle.

Movie S7. Automatic metastable assembly of "C" shape pieces.

References (*33*–*36*)

REFERENCES AND NOTES

1. A. Barbot, H. Tan, M. Power, F. Seichepine, G.-Z. Yang, Floating magnetic microrobots for fiber functionalization. *Sci. Robot.* **4**, eaax8336 (2019).
2. A. Pena-Francesch, J. Giltinan, M. Sitti, Multifunctional and biodegradable self-propelled protein motors. *Nat. Commun.* **10**, 3188 (2019).

3. F. Ongaro, S. Scheggi, A. Ghosh, A. Denasi, D. H. Gracias, S. Misra, Design, characterization and control of thermally-responsive and magnetically-actuated micro-grippers at the air-water interface. *PLOS ONE* **12**, e0187441 (2017).
4. K. Furukawa, T. Teshima, Y. Ueno, Self-propelled ion gel at air-water interface. *Sci. Rep.* **7**, 9323 (2017).
5. M. Dkhil, M. Kharboutly, A. Bolopion, S. Régnier, M. Gauthier, Closed-loop control of a magnetic particle at the air–liquid interface. *IEEE Trans. Autom. Sci. Eng.* **14**, 1387–1399 (2015).
6. M. Mastrangeli, S. Abbasi, C. Varel, C. Van Hoof, J.-P. Celis, K. F. Böhringer, Self-assembly from milli- to nanoscales: Methods and applications. *J. Micromech. Microeng.* **19**, 083001 (2009).
7. Y. S. Song, M. Sitti, Surface-tension-driven biologically inspired water strider robots: Theory and experiments. *IEEE Trans. Robot.* **23**, 578–589 (2007).
8. X. Zhang, J. Zhao, Q. Zhu, N. Chen, M. Zhang, Q. Pan, Bioinspired aquatic microrobot capable of walking on water surface like a water strider. *ACS Appl. Mater. Interfaces* **3**, 2630–2636 (2011).
9. O. Ozcan, H. Wang, J. D. Taylor, M. Sitti, Stride II: A water strider-inspired miniature robot with circular footpads. *Int. J. Adv. Robot. Syst.* **11**, 85 (2014).
10. J. H. Yan, X. B. Zhang, J. Zhao, G. F. Liu, H. G. Cai, Q. M. Pan, A miniature surface tension-driven robot using spatially elliptical moving legs to mimic a water strider's locomotion. *Bioinspir. Biomim.* **10**, 046016 (2015).
11. G. Lucarini, V. Iacovacci, P. J. Gouveia, L. Ricotti, A. Menciassi, Design of a novel magnetic platform for cell manipulation. *J. Micromech. Microeng.* **28**, 025009 (2018).
12. T. Yao, N. G. Chisholm, E. B. Steager, K. J. Stebe, Directed assembly and micromanipulation of passive particles at fluid interfaces via capillarity using a magnetic microrobot. *Appl. Phys. Lett.* **116**, 043702 (2020).
13. C. Pawashe, S. Floyd, M. Sitti, Multiple magnetic microrobot control using electrostatic anchoring. *Appl. Phys. Lett.* **94**, 164108 (2009).
14. E. Diller, J. Giltinan, M. Sitti, Independent control of multiple magnetic microrobots in three dimensions. *Int. J. Robot. Res.* **32**, 614–631 (2013).
15. A. Denasi, S. Misra, Independent and leader–follower control for two magnetic micro-agents. *IEEE Robot. Autom. Lett.* **3**, 218–225 (2017).
16. A. Marchand, J. H. Weijs, J. H. Snoeijer, B. Andreotti, Why is surface tension a force parallel to the interface? *Am. J. Phys.* **79**, 999–1008 (2011).
17. D. Vella, Floating versus sinking. *Annu. Rev. Fluid Mech.* **47**, 115–135 (2015).
18. L. E. Scriven, C. V. Sternling, The Marangoni effects. *Nature* **187**, 186–188 (1960).
19. J. W. Bush, D. L. Hu, Walking on water: Biolocomotion at the interface. *Annu. Rev. Fluid Mech.* **38**, 339–369 (2006).
20. N. Bassik, B. T. Abebe, D. H. Gracias, Solvent driven motion of lithographically fabricated gels. *Langmuir* **24**, 12158–12163 (2008).
21. J. H. Park, S. Lach, K. Polev, S. Granick, B. A. Grzybowski, Metal–organic framework "swimmers" with energy-efficient autonomous motility. *ACS Nano* **11**, 10914–10923 (2017).
22. C. Luo, H. Li, X. Liu, Propulsion of microboats using isopropyl alcohol as a propellant. *J. Micromech. Microeng.* **18**, 067002 (2008).
23. L. Zhang, Y. Yuan, X. Qiu, T. Zhang, Q. Chen, X. Huang, Marangoni effect-driven motion of miniature robots and generation of electricity on water. *Langmuir* **33**, 12609–12615 (2017).
24. M. A. Rahman, J. Cheng, Z. Wang, A. T. Ohta, Cooperative micromanipulation using the independent actuation of fifty microrobots in parallel. *Sci. Rep.* **7**, 3278 (2017).
25. W. Hu, Q. Fan, A. T. Ohta, An opto-thermocapillary cell micromanipulator. *Lab Chip* **13**, 2285–2291 (2013).
26. A. S. Basu, Y. B. Gianchandani, A programmable array for contact-free manipulation of floating droplets on featureless substrates by the modulation of surface tension. *J. Microelectromech. Syst.* **18**, 1163–1172 (2009).
27. R. Terrazas, A. Bolopion, J.-C. Beugnot, P. Lambert, M. Gauthier, Closed-loop particle motion control using laser-induced thermocapillary convective flows at the fluid/gas interface at micrometric scale. *IEEE/ASME Trans. Mech.* **23**, 1543–1554 (2018).
28. P. A. Kralchevsky, V. N. Paunov, I. B. Ivanov, K. Nagayama, Capillary meniscus interaction between colloidal particles attached to a liquid–fluid interface. *J. Colloid Interface Sci.* **151**, 79–94 (1992).
29. D. Vella, P. D. Metcalfe, R. J. Whittaker, Equilibrium conditions for the floating of multiple interfacial objects. *J. Fluid Mech.* **549**, 215–224 (2006).
30. N. Bowden, A. Terfort, J. Carbeck, G. M. Whitesides, Self-assembly of mesoscale objects into ordered two-dimensional arrays. *Science* **276**, 233–235 (1997).
31. M. Poty, G. Lumay, N. Vandewalle, Customizing mesoscale self-assembly with three-dimensional printing. *New J. Phys.* **16**, 023013 (2014).
32. P. Morin, C. Samson, Motion control of wheeled mobile robots. *Handbook Robot.* **1**, 799–826 (2008).
33. Dortmund data bank, http://www.ddbst.com [accessed 15 April 2020].
34. H. Chraïbi, J.-P. Delville, Thermocapillary flows and interface deformations produced by localized laser heating in confined environment. *Phys. Fluids* **24**, 032102 (2012).
35. J. E. Bertie, Z. Lan, Infrared intensities of liquids XX: The intensity of the OH stretching band of liquid water revisited, and the best current values of the optical constants of H_2O (l) at 25°C between 15,000 and 1 cm^{-1}. *Appl. Spectrosc.* **50**, 1047–1057 (1996).
36. E. H. Lucassen-Reynders, A. Cagna, J. Lucassen, Gibbs elasticity, surface dilational modulus and diffusional relaxation in nonionic surfactant monolayers. *Colloids Surf. A Physicochem. Eng. Asp.* **186**, 63–72 (2001).

Acknowledgments: We thank O. Stephan for the digital light printing of the multiple-legged robots, S. Dehaeck for providing help with the software and the image analysis algorithm, and R. Terrazas for the design of the optical system and fruitful discussions on the control laws. **Funding:** This work was funded by BELSPO (IAP 7/38 MicroMAST), FNRS grant (PDR T.0129.18), and the EUR EIPHI program (Contract No. ANR-17-EURE-0002). **Author contributions:** F.N.P.B. performed the flow numerical simulations, developed the ThermoBot dynamic model, implemented the control law for the different objects, and performed the experimental tests. A.B. and M.G. assisted F.N.P.B. in the development of the control laws, proposed the different experimental tests, and supervised the project. P.L. assisted F.N.P.B. in understanding and modeling the physics of the problem, initiated the project, secured funding, and supervised all steps of the project. **Competing interests:** The authors declare that they have no competing interests. **Data and materials availability:** All data needed to evaluate the conclusions in the paper are present in the paper and/or the Supplementary Materials.

Submitted 24 July 2020
Accepted 3 March 2021
Published 31 March 2021
10.1126/scirobotics.abd3557

Citation: F. N. Piñan Basualdo, A. Bolopion, M. Gauthier, P. Lambert, A microrobotic platform actuated by thermocapillary flows for manipulation at the air-water interface. *Sci. Robot.* **6**, eabd3557 (2021).

Science Robotics

A microrobotic platform actuated by thermocapillary flows for manipulation at the air-water interface

Franco N. Piñan Basualdo, A. Bolopion, M. Gauthier, and P. Lambert

Sci. Robot. **6** (52), eabd3557. DOI: 10.1126/scirobotics.abd3557

Science Robotics (ISSN 2470-9476) is published by the American Association for the Advancement of Science. 1200 New York Avenue NW, Washington, DC 20005. The title *Science Robotics* is a registered trademark of AAAS.